Evolutionary rewiring of host metabolism and interferon signalling by SARS-CoV-2 variants

Riaz-Ali Somji[1†], Jonathan C Brown[2†], Shahid Rowles-Khalid[3,4], Tukur Abdullahi[1], Dongsheng Luo[1], Natalie Barthel[5], Michael Mülleder[6], Markus Ralser[5], Wendy S Barclay[2‡], Charalampos Rallis[7‡], Efstathios S Giotis[1,2‡*]

[1]School of Life Sciences, University of Essex, Colchester, UK

[2]Department of Infectious Diseases, School of Medicine, Imperial College London, London, UK

[3]EGA Institute for Women's Health, Faculty of Population Health Sciences and Department of Mathematics, University College London, London, UK

[4]Department of Metabolism, Digestion and Reproduction, Imperial College London, London, UK

[5]Department of Biochemistry, Charité - Universitätsmedizin Berlin, Berlin, Germany

[6]Core Facility High Throughput Mass Spectrometry, Charité – Universitätsmedizin. Berlin, Germany

[7]Research Centre for Molecular Cell Biology, School of Biological and Behavioural Sciences, Queen Mary, University of London, London, UK

[†]Joint first authors

[‡]Corresponding authors with emails.

*Lead contact

Summary

SARS-CoV-2 variants differ in transmissibility and immune evasion, but their effects on host-cell metabolism and signalling remain less defined. Using integrated transcriptomic, phosphoproteomic, and amino acid profiling in primary nasal epithelial cells, we compared early and late host responses to pre-Omicron variants (Alpha, Beta), Delta, and Omicron subvariants (BA.1, BA.5). Pre-Omicron strains broadly suppressed antiviral interferon-stimulated gene expression and reprogrammed metabolism by reducing mitochondrial oxidative phosphorylation and β-oxidation. Delta infection was associated with extensive transcriptional and metabolic remodelling, characterised by activation of stress- and growth-related kinases and selective retention of biosynthetic amino acids, consistent with a host response to stress and viral modulation of interferon-associated signalling. In contrast, Omicron infection elicited a more restrained response dominated by cytokine and survival pathways, with limited metabolic activation and interferon suppression. Together, these findings suggest SARS-CoV-2 has progressively evolved toward a strategy that maintains efficient upper-airway replication while minimising epithelial stress and inflammation.

Keywords: SARS-CoV-2 variants, interferon-stimulated genes, metabolic reprogramming, nasal epithelial cells, host-pathogen interactions

Introduction

43 SARS-CoV-2, the causative agent of COVID-19, has evolved into multiple variants with distinct
44 transmissibility, immune evasion capacity, and associated disease severity. The successive
45 waves of Variants of Concern (VOCs), including Alpha (PANGO lineage B.1.1.7), Beta (B.1.351),
46 Delta (B.1.617.2/AY sublineages), and the many Omicron sublineages (B.1.1.529/BA
47 sublineages, such as BA.1, BA.2, and BA.5), exhibit distinct phenotypic characteristics and
48 transmission advantages over preceding variants. These advantages are largely driven by
49 genetic changes in the viral genome, particularly in the spike protein, which enhanced
50 receptor binding affinity and immune escape (Carabelli *et al*., 2023; Harvey *et al.*, 2021; Liu
51 and Rocklov, 2021). Additionally, VOCs exhibit varying capacities to suppress innate immune
52 responses, a key determinant of early viral control and disease progression (Carabelli *et al.*,
53 2023; Harvey *et al.*, 2021; Laine *et al.*, 2022; Reuschl *et al*., 2024).
54 The nasal epithelium serves as the primary entry site for SARS-CoV-2 infection and plays a
55 critical role in shaping early host responses (Shi *et al.*, 2024; Sungnak *et al.*, 2020). Nasal
56 epithelial cells (NECs) serve as both the primary site of viral entry and replication and as an
57 essential frontline of antiviral immunity, producing interferons (IFNs), a family of cytokines
58 that coordinate antiviral defence (Desmyter *et al*., 1968; Sposito *et al.*, 2021). Type I (e.g., IFN-
59 α and IFN-β) and type III (e.g., IFN-λ) interferons bind to their respective receptors on infected
60 and neighbouring cells, triggering the Janus kinase/signal transducer and activator of
61 transcription (JAK-STAT) pathway. Type II interferon (IFN-γ), primarily derived from immune
62 effector cells, complements these pathways by amplifying antiviral and immunomodulatory
63 responses once immune infiltration occurs. This leads to the induction of hundreds of
64 interferon-stimulated genes (ISGs), which act collectively to inhibit viral replication, degrade
65 viral RNA, and enhance antigen presentation (Park and Iwasaki, 2020; Schneider *et al*., 2014).
66 SARS-CoV-2 has evolved multiple strategies to suppress these IFN responses, thereby evading

early immune detection and promoting viral persistence (Carabelli *et al.*, 2023; V'Kovski *et al.*, 2021; Yuen *et al.*, 2020). The Alpha and Beta strains inhibit IFN production more effectively than earlier reference strains (Gori Savellini *et al.*, 2023; Rajah *et al.*, 2021). Delta, in contrast, displays enhanced replication efficiency and greater host immune antagonism, leading to higher viral loads and increased disease severity (Liu and Rocklov, 2021; Rajah *et al.*, 2021). In comparison, several studies suggest that Omicron subvariants exhibit a reduced interaction with the interferon response, although some evidence indicates a delayed yet stronger induction of ISGs (Gori Savellini *et al.*, 2023; Laine *et al.*, 2022; Shi *et al.*, 2024). Collectively, these findings suggest that each variant has evolved unique strategies to modulate IFN signalling and evade early antiviral defenses.

Among the emerging variants, Omicron variants remain globally dominant, as they rapidly displaced previous VOCs, through successive waves of transmission. Unlike earlier SARS-CoV-2 variants, Omicrons show an increased preference for the upper airways and a reduced transition to the lower respiratory tract (Shi *et al.*, 2024). Studies suggest that mutations in the Omicron spike protein enhance viral entry into nasal epithelial cells, enabling evasion of both constitutive and interferon-induced antiviral factors that normally limit SARS-CoV-2 entry following attachment (Gori Savellini *et al.*, 2023; Reuschl *et al.*, 2024; Shi *et al.*, 2024). In contrast to previous variants that predominantly rely on serine transmembrane proteases for host cell entry, Omicron strains preferentially use cysteine proteases cathepsin B (CatB) and cathepsin L (CatL) to catalyse endosomal membrane fusion, possibly providing an advantage in nasal epithelial infection and potentially contributing to their increased respiratory transmissibility (Giotis *et al.*, 2022; Leach *et al.*, 2021; Shi *et al.*, 2024). These adaptations in entry mechanisms and tissue tropism raise important questions about how variant-specific traits impact downstream host cellular responses.

While extensive research on VOCs has focused on spike protein mutations and their role in enhancing viral entry and immune evasion, much less is known about how these variants differentially reprogram host cell metabolism and signalling to optimise replication and immune escape. Viruses such as Influenza A, Dengue, HBV, HIV and others typically hijack host metabolic networks to create an environment conducive to replication, altering energy production, amino acid biosynthesis, and lipid metabolism to support viral genome replication, protein synthesis, and virion assembly (Allen *et al.*, 2022; Chan *et al.*, 2009; Liu *et al.*, 2020; Long *et al*., 2016; Polcicova *et al*., 2020; Ritter *et al*., 2010; Singh *et al.*, 2020; Thaker *et al.*, 2019). Current understanding of SARS-CoV-2 metabolic reprogramming largely derives from studies on early variants**,** which have shown that the virus targets key pathways such as glycolysis, the tricarboxylic acid (TCA) cycle, and the pentose phosphate pathway (PPP) to meet biosynthetic and redox demands (Codo *et al.*, 2020; Guarnieri *et al.*, 2024; Mullen *et al.*, 2021). A central hallmark of this reprogramming leading to the accumulation of mitochondrial reactive oxygen species (mROS) and consequent oxidative stress is the inhibition of mitochondrial oxidative phosphorylation (OXPHOS) (Guarnieri *et al.*, 2024)**.** Elevated mROS stabilises hypoxia-inducible factor 1-alpha (HIF-1α)**,** a key regulator that redirects cellular metabolism toward glycolysis and the PPP, enhancing the synthesis and mobilisation of nucleotides, lipids, and amino acids, which are necessary for viral replication (Guarnieri *et al.*, 2024; Mullen *et al.*, 2021). The virus also activates the mechanistic target of rapamycin complex 1 (mTORC1) and integrated stress response (ISR) pathways, which in-turn promote nutrient uptake, glycolysis, and innate immune signalling, while suppressing mitochondrial biogenesis and cytosolic protein synthesis (Guarnieri *et al.*, 2024; Li *et al.*, 2021; Mullen *et al.*, 2021; Zambalde *et al*., 2022). In parallel, the virus disrupts cellular stress responses and modulates key signalling pathways, such as the phosphoinositide 3-kinase/protein kinase B

115 (PI3K/AKT) and mitogen-activated protein kinase (MAPK) pathways, to promote cell survival
116 (Bojkova *et al.*, 2020; Li *et al.*, 2021; V'Kovski *et al.*, 2021). Despite these insights from early
117 variants, how such metabolic and signalling circuits have been refined or rewired in later
118 variants, particularly Delta and Omicron, remains poorly understood.
119
120 In this study, we focused on six epidemiologically and biologically representative SARS-CoV-2
121 lineages, which capture the principal stages of viral adaptation in replication dynamics,
122 immune evasion, and host metabolic engagement during the pandemic. Using an integrated
123 multi-omics approach in primary human nasal epithelial cells cultured at the air-liquid
124 interface, we compared their transcriptional, signalling, and metabolic responses at early and
125 late stages of infection to define lineage-specific strategies of host manipulation and their
126 implications for viral fitness and adaptation.
127
128 **Results**
129 Understanding how SARS-CoV-2 variants remodel host cell metabolism and signalling is
130 critical to deciphering their evolutionary adaptations in transmissibility and immune evasion.
131 To investigate these processes, primary nasal epithelial cells (NECs) from a pool of human
132 donors were cultured at the air-liquid interface and infected with three classes of SARS-CoV-
133 2 variants: early strains (IC19 (a lineage B.1 SARS-CoV-2 reference strain), the pre-Omicron:
134 Alpha, Beta), Delta, and Omicron subvariants (BA.1, and BA.5). NECs were derived from three
135 commercially available donor pools (MucilAir™, Epithelix), each comprising epithelial cells
136 from 10-14 independent human donors. This pooled design ensured physiological relevance
137 and helped minimise donor-specific variability across infection conditions. Viral replication
138 kinetics were measured over 72 hours. Transcriptomic analysis (RNA-seq) was conducted at

139 24 and 72 hpi, and phosphoproteomic and amino acid profiling were performed at 24 hpi to
140 characterise early post-translational and metabolic responses (Figure 1A).
141
142 **Omicron and Delta variants exhibit increased replication compared to pre-Omicron strains**
143 To compare the replication dynamics of SARS-CoV-2 variants, NECs were infected with the
144 variants at a multiplicity of infection (MOI) of 0.01, and viral genome copies in the culture
145 supernatants were quantified over time using *E* gene RT-qPCR (Figure 1B).
146 At 24 hpi, BA.1 exhibited the highest early replication, with significantly elevated viral genome
147 copies compared to the pre-Omicron reference strain IC19 ($p < 1 \times 10^{-4}$), indicating an early
148 replication advantage. By 48 and 72 hpi, Delta showed the highest viral loads, significantly
149 exceeding IC19 at both time points ($p = 1.4 \times 10^{-3}$ and 2.9×10^{-3}, respectively). BA.5 and Beta
150 also demonstrated increased replication relative to IC19, with significantly higher viral titres
151 at 48 hpi ($p = 1.65 \times 10^{-2}$ and 1.73×10^{-2}) and 72 hpi ($p = 2.61 \times 10^{-2}$ and 2.88×10^{-2}). These
152 findings demonstrate group-specific replication dynamics, with Delta and Omicron
153 subvariants exhibiting increased replication efficiency in nasal epithelial cells compared to
154 pre-Omicron strains.
155
156 **Delta triggers the most extensive transcriptional remodelling late in infection**
157 To characterise host transcriptional responses to SARS-CoV-2 variants, we performed RNA-
158 seq on NECs at 24 and 72 hpi (Figure 2A-C). Differentially expressed genes (DEGs) were
159 defined by a $\log_2$ fold change ≥ |1| and FDR ≤ 0.05 (Table S1).
160 At 24 hpi, pre-Omicron variants (IC19, Alpha, and Beta) elicited the most substantial early
161 responses, with Alpha alone triggering over 3,800 DEGs (645 up-regulated, 3,162 down-

162 regulated). In contrast, Delta and the Omicron subvariants (BA.1 and BA.5) triggered markedly
163 fewer changes, suggesting attenuated or delayed early sensing (Figure 2B).
164 By 72 hpi, Delta drove the most extensive transcriptional reprogramming across all variants
165 (1,242 up-regulated, 4,432 down-regulated genes), while BA.1 and BA.5 induced intermediate
166 responses. Although some overlap in down-regulated genes was observed between Delta and
167 Omicron, the majority of DEGs remained variant-specific (Figure 2C).
168 Together, these data reveal distinct temporal transcriptional patterns across SARS-CoV-2
169 variants, with Delta driving the broadest late-stage reprogramming and highlighting the
170 evolving diversity of host–virus interactions.

171 **Reduced suppression of host interferon responses following infection with Omicron**
172 **subvariants**

173 We next examined how SARS-CoV-2 variants modulate innate antiviral signalling by
174 measuring interferon-stimulated gene (ISG) expression in primary nasal epithelial cells at 24
175 and 72 hpi (Figure 3A–D). ISGs represent core effectors of the type I interferon pathway and
176 provide a transcriptional readout of antiviral activation (Park and Iwasaki, 2020) (Figure 3A).
177 Cells treated with recombinant interferon alpha (IFN-α) were included as a reference to
178 establish a benchmark for ISG induction.
179 At 24 hpi, ISG induction remained low across all variant-infected relative to mock samples
180 (Figure 3B). Alpha and Beta showed the weakest early responses, whereas Delta and the
181 Omicron subvariants BA.1 and BA.5 triggered modest but detectable up-regulation. By 72 hpi,
182 ISG expression was broadly elevated, but with clear variant-specific differences (Figure 3C).
183 BA.1 and BA.5 induced the largest and most diverse ISG repertoires, similar in scale to those
184 induced by IFN-α, while Alpha and Beta exhibited more restricted activation. In contrast, Delta

185 consistently induced the fewest ISGs, even as infection advanced, pointing to sustained
186 suppression of interferon responses.
187 A heatmap of the top 30 IFN-α-responsive ISGs (Figure 3D) further illustrates these
188 differences. BA.1 and BA.5 displayed relatively higher expression of canonical antiviral genes
189 by 72 hpi such as *CXCL10*, *ISG15*, *IFIT1*, and *OAS1*, key effectors of RNA sensing, translational
190 arrest, and immune recruitment (Schneider *et al.*, 2014; Schoggins, 2019; Schoggins *et al.*,
191 2011), compared with Delta. Compared with BA.1- and BA.5-infected cells, Delta-infected
192 cells showed fewer IFN-α–responsive genes and reduced expression levels, suggesting a
193 weaker activation of interferon signalling.
194
195 **Progressive tuning of host metabolism from early lineages to Delta and Omicron**
196 Previous reports have shown that early SARS-CoV-2 lineages, including IC19, Alpha, and Beta,
197 are associated with reduced mitochondrial activity and enhanced glycolytic flux, an
198 established viral strategy to redirect cellular resources toward biosynthesis (Codo *et al.*, 2020;
199 Guarnieri *et al.*, 2024; Mullen *et al.*, 2021). Cytosolic pathways such as glycolysis and the
200 pentose phosphate pathway (PPP) generate biosynthetic precursors, whereas mitochondrial
201 metabolism, including the tricarboxylic-acid (TCA) cycle, fatty-acid oxidation (FAO), and
202 oxidative phosphorylation (OXPHOS), supports ATP production, redox balance, and antiviral
203 signalling.
204 To investigate how infection with different SARS-CoV-2 variants correlates with metabolic
205 pathway changes in host cells, we performed gene set enrichment analysis (GSEA) of RNA-
206 seq data from NECs infected with the variants at 24 and 72 hpi, relative to uninfected controls
207 (Figure 4A-B). Normalised enrichment scores (NES) were used to quantify coordinated
208 transcriptional changes across curated metabolic pathways, providing a comparative measure

209 of pathway activation (positive NES) or suppression (negative NES) independent of gene-set
210 size and variance (Figure 4; full data is listed in Table S2). For interpretation, pathways with
211 an FDR < 0.05 were categorised by NES magnitude as follows: |NES| < 1.0, limited enrichment;
212 1.0 ≤ |NES| < 1.8, moderate enrichment; |NES| ≥ 1.8, strong enrichment.
213 At 24 hpi, metabolic responses were limited in magnitude (Figure 4A). Cells infected with most
214 variants showed near-neutral or mildly positive NES values in glycolysis and PPP, suggesting
215 modest early cytosolic engagement. FAO gene sets were consistently negative across
216 lineages, indicating an early block in β-oxidation. Mitochondrial carrier and import modules
217 were close to neutral, while OXPHOS complexes displayed small but generally positive
218 enrichment, apart from a minor negative signal in the Alpha/Beta Complex IV module. Thus,
219 early infection was associated with preserved or moderately enhanced respiratory-gene
220 expression rather than broad suppression.
221 By 72 hpi, clear lineage-specific profiles emerged (Figure 4B). Delta-infected cells exhibited
222 the highest and most coordinated positive NES across OXPHOS complexes I–V and several
223 mitochondrial modules, indicating strong respiratory activation accompanied by moderate
224 enrichment of glycolytic and lipid-metabolism pathways. Cells infected with the reference
225 strain IC19 retained moderate OXPHOS activation. Cells infected with pre-Omicron strains
226 displayed overall weaker enrichment and more variable mitochondrial responses. In contrast,
227 Omicron-infected cells showed near-neutral cytosolic NES, negative FAO and coenzyme Q
228 biosynthesis scores, and modest positive enrichment of mitochondrial-carrier and OXPHOS
229 modules, again with a negative Complex IV component. These findings suggest that Omicron
230 infection elicits a host response that maintains basal mitochondrial function while avoiding
231 extensive metabolic activation.

232 Grouped comparison (Figure 4B) summarises these three variant-specific trends. Cells
233 infected with early lineages (IC19, Alpha, Beta) show moderate OXPHOS enrichment at 24 hpi
234 that diminishes and becomes variable by 72 hpi. Delta-infected cells display the strongest and
235 most coordinated activation across respiratory and associated metabolic pathways. Omicron-
236 infected cells retain a selective, mitochondria-centred profile with positive overall OXPHOS
237 and minimal cytosolic activation.
238
239 **Delta activates stress kinases, while Omicron reprograms cytokine and survival signalling**
240 To characterise early host signalling responses, we profiled phosphorylation events at 24 hpi
241 in NECs infected with IC19, Delta, BA.1, and BA.5 using phospho-kinase arrays. These variants
242 were selected to represent the most distinct host-response patterns observed in our dataset:
243 IC19 as the ancestral reference, Delta as the lineage that showed the broadest transcriptional
244 and metabolic engagement in infected cells, and BA.1/BA.5 as Omicron subvariants that, in
245 our system, elicited comparatively restrained early responses but clearer cytokine-linked
246 signalling at later stages. Phosphorylation levels were normalised to mock controls, and
247 statistical significance was assessed using Welch's *t*-tests with Benjamini–Hochberg
248 correction (FDR < 0.05; Table S3).
249 Relative to mock, all infections were associated with phosphorylation changes in stress-,
250 growth-, and cytokine-associated proteins, but the magnitude and pattern differed markedly
251 between variants (Figure 5A–B). Compared with IC19-, Delta-infected cells displayed the
252 most extensive activation of cellular stress and translational pathways, with significant
253 increases in p53, PRAS40, and p70 kinase alongside higher phosphorylation of STAT3 and
254 STAT6. This profile suggests enhanced engagement of stress-responsive and translational
255 signalling pathways**.** Collectively, the pattern observed in Delta-infected cells is consistent

256 with a stress-associated and pro-survival phosphorylation signature dominated by the p53–
257 RSK–S6K and PRAS40 nodes.
258 By contrast, cells infected with Omicron subvariants exhibited phosphorylation patters
259 enriched in immune- and cytokine-linked pathways. BA.1-infected cells showed prominent
260 phosphorylation of p38 MAPK, PLC-γ1, RYK, and Src, alongside strong activation of JAK–STAT
261 components including STAT1, STAT2, and STAT5. Phosphorylation fold changes for STAT1
262 (11.7-fold) and STAT2 (4.0-fold) were the highest among all variants, consistent with strong
263 interferon- and cytokine-associated signalling. Cells infected with BA.5 showed a similar but
264 overall attenuated profile compared with BA.1, retaining phosphorylation of the p53, STAT3
265 (S727), and Src-family kinases.
266
267 **Contrasting host amino acid regulation by Delta and Omicron variants**
268 To complement the transcriptomic and phosphoproteomic analyses, intracellular amino acid
269 levels were quantified at 24 hpi in nasal epithelial cells infected with IC19, Delta, BA.1 or BA.5
270 and compared with mock-infected controls (Figure 6; Table S4). Total intracellular amino acid
271 abundance (Figure 6A) showed modest, non-significant reductions in IC19- and Delta-infected
272 cells ($q > 0.05$), despite an approximate 10% decrease in IC19 relative to mock. In contrast,
273 BA.1- and BA.5-infected cells exhibited significant reductions in total amino acid pools ($q <$
274 0.01 and $q < 0.05$, respectively). All amino acid measurements were expressed as nmol per
275 10^6 viable, counted cells, and viability at 24 hpi was comparable across conditions, indicating
276 that differences in abundance reflect infection-driven metabolic changes rather than
277 variation in cell number.
278 The variant–amino acid interaction network (Figure 6B) visualises these differences by linking
279 each variant to its most strongly altered amino acids. Edge width reflects the absolute $\log_2$

280 fold change, and colour indicates direction (red for increases, blue for decreases relative to
281 mock). BA.1 and BA.5 display numerous, broad negative edges, while IC19 and Delta show
282 fewer, thinner connections, consistent with a more limited metabolic impact.
283 Individual amino acid profiles (Figure 6C; Table S4) further resolved these patterns. In BA.1-
284 infected cells, intracellular amino acid levels showed the broadest and most significant
285 reductions, including all branched-chain and aromatic amino acids (leucine, phenylalanine,
286 tryptophan, isoleucine, valine), together with decreases in several other amino acids,
287 including threonine, serine, arginine and lysine. BA.5-infected cells exhibited a similar but less
288 pronounced profile, with significant decreases in many essential amino acids and moderate
289 increases in alanine and proline. Delta-infected cells displayed a mixed pattern, characterised
290 by significant increases in proline, alanine, glycine and glutamine, alongside reductions in
291 selected essential amino acids such as isoleucine and phenylalanine. IC19-infected cells
292 showed only small, variable changes, none of which reached significance after FDR correction.
293 To examine whether infection altered the internal balance of amino acids rather than total
294 abundance, amino acid levels were normalised to the total amino acid content within each
295 condition (Figure 6D; Table S4). The relative amino acid composition appeared consistent
296 across variants, suggesting that infection reduces overall amino acid availability without
297 disturbing the proportional balance within the intracellular pool.
298 Together, these data show that amino acid abundances in variant-infected cells differ from
299 those in mock-infected cells in a lineage-specific manner, with Delta-infected cells showing
300 comparatively higher levels of several biosynthetically relevant amino acids, whereas cells
301 infected with Omicron subvariants display broad amino acid depletion and limited
302 compensatory increases across pathways. Amino acids are central to energy production,

303 redox balance, protein synthesis, and immune signalling, and their intracellular abundance
304 provides a sensitive readout of metabolic stress and viral resource use (Thaker *et al.*, 2019).
305
306 **Discussion**
307 SARS-CoV-2 variants have evolved distinct capacities to replicate, modulate host immunity,
308 and influence disease severity. Although mechanisms of viral entry and antibody escape are
309 well characterised, far less is understood about how major lineages remodel host cellular
310 pathways once infection is established. To address this, we employed differentiated nasal
311 epithelial cells (NECs) grown at air-liquid interface, a physiologically relevant model that
312 recapitulates early epithelial infection in the absence of systemic immune influences. This
313 system enables direct examination of variant-specific host responses at the primary site of
314 replication, which may differ in magnitude and kinetics from those observed in bronchial or
315 immune-cell containing models. Through an integrated multi-omics approach, we uncovered
316 lineage-specific differences in the extent, timing, and coordination of transcriptional,
317 signalling, and metabolic responses.
318
319 Early lineages (IC19, Alpha, Beta) broadly down-regulated immune and metabolic transcripts
320 at 24 hpi, consistent with potent suppression of innate antiviral signalling. These results align
321 with previous studies showing that early SARS-CoV-2 isolates suppress mRNA synthesis and
322 translation through ORF6-, ORF8-, and ORF9b-mediated interference with STAT1/2 and
323 nuclear import (Laine *et al.*, 2022; Reuschl *et al.*, 2024; V'Kovski *et al.*, 2021; Yuen *et al.*, 2020).
324 By 72 hpi, infected nasal epithelial cells exhibited clear lineage-specific divergence. Cells
325 infected with Delta exhibited extensive transcriptional reprogramming, including activation
326 of stress-response, metabolic, and cytokine-related genes. In contrast, Omicron-infected cells

327 displayed fewer differentially expressed genes, nevertheless, showed selective enrichment of
328 interferon-stimulated and cytokine-responsive transcripts, consistent with a delayed yet
329 measurable antiviral response (Gori Savellini *et al.*, 2023; Reuschl *et al.*, 2024; Shi *et al.*, 2024).
330 Consistent with previously reported effective antagonism of RIG-I/MDA5–JAK–STAT signalling
331 (Laine *et al.*, 2022; Sievers *et al.*, 2024; Tandel *et al.*, 2022) IC19, Alpha, Beta, and Delta
332 displayed weak ISG induction at both 24 and 72 hpi. In contrast, Omicron elicited a broader
333 ISG response by 72 hpi, approaching that observed following exogenous IFN-α treatment,
334 suggesting only partial suppression of interferon-driven transcription (Reuschl *et al.*, 2024; Shi
335 *et al.*, 2024).
336 Phosphoproteomic profiling further distinguished variant phenotypes. Omicron infections
337 enhanced phosphorylation within JAK–STAT and MAPK modules (STAT1/2/5, p38, PLC-γ1,
338 Src), while Delta preferentially activated stress- and growth-associated kinases (p53, PRAS40,
339 RSK, p70 S6K), indicating engagement of PI3K–Akt–mTORC1 and the integrated stress
340 response (Bouhaddou *et al.*, 2020; Klann *et al.*, 2020; Li *et al.*, 2021). These patterns suggest
341 that Omicron can replicate despite ongoing cytokine signalling, whereas Delta infection
342 favours stress- and growth-linked pathways to sustain replication.
343 Our metabolic data reveal pronounced lineage-specific differences in host–virus
344 interaction. Consistent with previous reports (Codo *et al.*, 2020; Mullen *et al.*, 2021), cells
345 infected with pre-Omicron lineages suppressed fatty-acid oxidation and exhibited modest,
346 heterogenous mitochondrial changes, indicating partial mitochondrial adaptation rather than
347 broad inhibition. Conversely, Delta-infected cells displayed the strongest and most
348 coordinated activation spanning oxidative-phosphorylation complexes I–V and several
349 mitochondrial modules, accompanied by moderate enrichment of cytosolic pathways,
350 including the tricarboxylic-acid cycle and lipid metabolism. These transcriptional shifts

351 occurred despite broadly comparable viral loads across lineages at 24-72 hpi, suggesting that
352 replication level alone does not account for the observed metabolic divergence. Delta-
353 infected NECs retained or modestly increased one-carbon intermediates such as glycine,
354 glutamine, and alanine, consistent with preserved anabolic and redox capacity. Targeted
355 metabolomic analysis further revealed that total intracellular amino acid pools declined
356 across infections relative to mock, but the extent varied by lineage: Delta-infected cells
357 exhibited the smallest reduction, BA.5-infected cells an intermediate profile, and BA.1-
358 infected cells the most pronounced depletion, particularly of essential and branched-chain
359 amino acids such as leucine and valine. These findings indicate that Delta sustains a more
360 biosynthetically active state, whereas Omicron subvariants replicate under more
361 metabolically constrained conditions, suggesting a shift towards a low-anabolism infection
362 strategy. When amino acid levels were normalised to total intracellular content, the overall
363 proportional balance of amino acids in variant-infected cells was largely preserved, with only
364 a small deviation detected for BA.1 compared with mock. This pattern suggests that SARS-
365 CoV-2 lineages primarily modulate the metabolic tone of nasal epithelial cells by altering
366 amino acid availability, rather than by extensively reshaping the internal composition of the
367 amino acid pool.
368 Integration of transcriptomic, phosphoproteomic, and metabolic datasets, delineates three
369 distinct host-virus interaction strategies. Early lineages dampened transcription, interferon
370 signalling, and fatty-acid oxidation while maintaining only minimal mitochondrial activity.
371 Delta, by contrast, exhibited coordinated activation of respiratory, cytosolic, and stress
372 pathways, consistent with higher metabolic demand. Omicron retained efficient replication
373 while preserving mitochondrial respiration and tolerating interferon-linked signalling, yet
374 engaging anabolic metabolism only weakly. These lineage-specific programmes likely reflect

375 not only viral genetic differences but also the interplay between replication dynamics and
376 epithelial sensing thresholds in NECs. Overall, SARS-CoV-2 evolution appears to have
377 progressively re-tuned the balance between replication, metabolism, and immune
378 modulation. Later variants replicate effectively while imposing a smaller metabolic load and
379 causing less epithelial stress, yet remain capable of replication in the presence of active
380 cytokine and interferon responses. This restrained, energy-efficient infection profile mirrors
381 clinical observations that Omicron replication is largely confined to the upper airways and
382 associated with reduced epithelial injury and inflammation (Carabelli *et al.*, 2023; Gori
383 Savellini *et al.*, 2023; Laine *et al.*, 2022).
384 The use of pooled donor–derived NECs enhances physiological relevance but may mask inter-
385 individual variation in antiviral and metabolic responses. Future studies sampling additional
386 time points and integrating isotope-tracing could define metabolic flux through glycolysis and
387 the TCA cycle, while targeted perturbation of pathways such as PI3K–Akt–mTORC1, p53–RSK–
388 S6K, and p38 MAPK in ALI cultures could establish causal links between signalling nodes and
389 replication outcomes. Extending the approach to lower-airway or immune–epithelial co-
390 culture models would further connect cellular rewiring to tissue-level phenotypes and
391 transmissibility.
392 In summary, SARS-CoV-2 variants employ distinct reprogramming strategies in nasal
393 epithelium. Pre-Omicron strains strongly suppress antiviral and metabolic responses; Delta
394 drives extensive activation of stress and energy pathways; Omicron maintains mitochondrial
395 activity while limiting broader metabolic engagement. These contrasting strategies illustrate
396 how viral evolution has refined replication efficiency relative to metabolic demand and
397 immune modulation, providing mechanistic insight for host-targeted therapeutic approaches.
398

399 **Resource Availability**

400 **Lead Contact**

401 Further information and requests for resources and reagents should be directed to and will
402 be fulfilled by the Lead Contact, Dr Efstathios Giotis (e.giotis@essex.ac.uk).

403 **Materials availability**

404 No new unique reagents or biological materials were generated in this study. SARS-CoV-2
405 variant strains were obtained from existing publicly available virus collections, as indicated in
406 the Materials and Methods. All cell lines and virus isolates used are commercially or
407 institutionally available.

408 **Data and code availability**

409 The RNA sequencing data generated during this study have been deposited in the Gene
410 Expression Omnibus (GEO) under accession number GSE271378. The phosphoproteomic and
411 amino acid profiling datasets are available in the Supplemental information and can also be
412 shared upon request from the Lead Contact. This study generated analysis scripts for figure
413 production, available upon reasonable request from the Lead Contact. Scripts for data
414 visualisation (e.g., R scripts for heatmaps, Python for statistical plots) are available from the
415 Lead Contact upon reasonable request.

416

417 **Author contributions**

418 E.S.G. conceptualised the study, supervised the project, and contributed to methodology,
419 investigation, formal analysis, visualisation, and funding acquisition. R.A.S., J.B., T.A., N.B.,
420 D.L. and M.Mu. performed experimental work and contributed to methodology and
421 investigation. S.R.K. carried out bioinformatic analyses, formal analysis, data curation, and
422 visualisation. R.A.S. also contributed to data visualisation. M.Ra. conducted amino acid

423 profiling and provided resources and supervision. W.S.B. and C.R. contributed to project
424 supervision, resources, and funding acquisition. E.S.G., R.A.S., and S.R.K. wrote the original
425 draft, and all authors reviewed and edited the manuscript.
426

427 **Acknowledgements**

428 We are grateful to Juhi Kumar, Dorothee Reuss, Natalia Paulina Twardowska and Tom
429 Peacock for their technical assistance and helpful input during manuscript preparation. This
430 work was supported by the University of Essex COVID-19 Rapid and Agile Fund and the Faculty
431 of Science and Health Research Innovation and Support Fund. EG and DL are funded by an
432 MRC New Investigator Research Grant (MR/Z506242/1) and the Royal Society
433 (RGS\R2\242527). C.R. acknowledges support and funding from the Biotechnology and
434 Biological Sciences Research Council [Research grant numbers: BB/V006916/1,
435 BB/V006916/2] and from the Medical Research Council [Grant number: MR/W001462/1].
436 Tukur Abdullahi is supported by the Nigerian Petroleum Technology Development Fund and
437 the University of Essex.

438 **Declaration of interests**

439 The authors declare no competing interests.

440 **Supplemental information**

441 **Supplementary Figures S1–S2**.

442 Contains validation of RNA-seq data by qPCR across selected immune signalling and
443 metabolic genes. Includes:

444 • **Supplementary Figure S1:** Correlation plot of RNA-seq vs qPCR fold-change values
445 for immune-signalling genes (*CXCL10, IFIT1, IFIT2, ISG15, OAS1, STAT1*).
446 • **Supplementary Figure S2:** Correlation plot of RNA-seq vs qPCR fold-change values
447 for metabolism-related genes (*HK2, GMPR, ENO2, MDH1B, ATP6V1B1*).

448 **Table S1.** Excel file containing DEG lists from RNA-sequencing analysis across SARS-CoV-2
449 variants, related to Figures 1 and 3.

450 **Table S2.** Normalised Enrichment Scores (NES) from fast Gene Set Enrichment Analysis
451 (fGSEA) of oxidative phosphorylation (OXPHOS), cytosolic and mitochondrial metabolic
452 pathways across SARS-CoV-2 variants and time points. NES, adjusted *p*-values (FDR), and
453 leading-edge gene counts are reported for each pathway.

454 **Table S3.** Excel file containing phospho-kinase array raw and processed data, related to
455 Figure 5.

456 **Table S4.** Excel file containing raw and normalised intracellular amino acid levels (nmol/10^6
457 cells), related to Figure 6.

458 **Table S5:** Primer sequences and RefSeq accession numbers used for qPCR validation.

459

460 **Figure Legends**

461 **Figure 1. Omicron and Delta variants exhibit enhanced replication compared to pre-**
462 **Omicron strains**

463 (**A**) **Schematic representation of the experimental setup.** Primary human nasal epithelial
464 cells were cultured at the air-liquid interface and infected with six SARS-CoV-2 variants: IC19
465 (reference strain), Alpha, Beta, Delta, Omicron BA.1, and Omicron BA.5. All infections were
466 performed at a multiplicity of infection (MOI) of 0.01. Parallel wells treated with recombinant
467 IFN-α served as a transcriptional benchmark. Cells were harvested at 24, 48, and 72 hpi for
468 downstream analyses, including phosphoproteomic profiling, amino acid (AA) profiling, and
469 RNA sequencing (RNA-seq). The timeline indicates the specific time points at which each
470 molecular analysis was conducted.
471 (**B**) **Growth kinetics of SARS-CoV-2 variants.** Viral replication over a 72-hour period was
472 quantified by RT-qPCR targeting the *E* gene. Viral RNA levels are expressed as *E* gene copies
473 per millilitre on a log10 scale. Measurements were taken at 0, 24, 48, and 72 hpi. Variants
474 Delta and BA.1 demonstrated significantly elevated viral loads compared to the reference
475 strain IC19 at multiple time points. Statistical significance was evaluated using one-way
476 ANOVA with Tukey's multiple comparisons test. Asterisks indicate significance levels: *$p <$
477 0.05, **$p < 0.01$, ***$p < 0.001$. Data are shown as mean ± standard deviation (SD) from three
478 independent experiments.
479
480 **Figure 2. Transcriptomic profiling of host responses to SARS-CoV-2 variant infection.**
481 (A) Number of significantly up-regulated (red) and down-regulated (blue) differentially
482 expressed genes (DEGs) at 24 and 72 hpi with indicated SARS-CoV-2 variants, based on RNA-
483 seq analysis (log2 fold-change ≥1; FDR <0.05).
484 (B) Venn diagrams showing shared and unique up-regulated DEGs among variants at 24 hpi
485 (top) and 72 hpi (bottom).
486 (C) Venn diagrams showing shared and unique down-regulated DEGs among variants at 24

487 hpi (top) and 72 hpi (bottom). Percentages represent overlap relative to the total DEGs per
488 variant.

489 **Figure 3. Late ISG induction by Omicron strains versus sustained attenuation by Delta**

490 (**A**) **Schematic of interferon signalling and ISG activation.**

491 (**B-C**) **Shared and unique ISG induction across variants at 24 (B) and 72 (C) hpi.** An UpSet plot
492 visualizes the number of significantly up-regulated ISGs (FDR < 0.05) per SARS-CoV-2 variant
493 and their overlaps. The bar chart at the top indicates the size of each intersection set, while
494 the connected dots below identify which variants contribute to each group. The colored
495 horizontal bars represent total ISG numbers detected per variant. The inset bar graphs show
496 the total number of significantly upregulated genes detected for each variant at the
497 corresponding time point, providing context for overall transcriptional activation.

498 (**D**) **Heatmaps showing log2 fold-change of top ISGs induced by IFNα treatment and during**
499 **infection at 24 and 72 hpi.** The leftmost panel shows the top ISGs up-regulated by IFNα
500 treatment alone, identifying baseline interferon responsiveness of the cells. The middle and
501 right panels show the expression of these ISGs in response to viral infection across all six SARS-
502 CoV-2 variants at 24 and 72 hpi, respectively. Color intensity reflects log2 fold-change, with
503 red indicating upregulation and blue indicating down-regulation or suppression.

504

505 **Figure 4. Normalised enrichment scores (NES) depict pathway-level transcriptional**
506 **changes across SARS-CoV-2 variants and time points.**

507 (**A**) Variant-specific NES profiles for cytosolic, mitochondrial, and oxidative phosphorylation
508 (OXPHOS) pathways at 24 and 72 hpi. Differential expression values (log_2 fold change) were
509 ranked and analysed with the fgsea R package using curated KEGG and literature-based
510 gene sets.

511 (**B**) Merged analysis comparing Pre-Omicron and Omicron lineages, showing composite NES
512 values summarizing transcriptional regulation across variants. Red indicates pathway
513 activation, blue indicates suppression. NES, normalised enrichment score.
514
515 **Figure 5. SARS-CoV-2 variants differentially regulate host signalling pathways through**
516 **phosphorylation events.**
517 (**A**) **Representative phospho-protein arrays** showing phosphorylation patterns in uninfected
518 mock controls and cells infected with IC19, Delta, Omicron BA.1, and Omicron BA.5 at 24
519 hpi. Key differentially phosphorylated proteins are highlighted.
520 (**B**) **Quantitative analysis of phosphorylation fold changes (variant-infected vs. mock)**
521 **across all array targets grouped by signalling pathway.** Dots represent mean values from at
522 least two independent experiments, with vertical error bars showing the standard error of
523 the mean (SEM). Colour coding denotes variant groups: IC19 (blue), Delta (orange), BA.1
524 (green), and BA.5 (red). Markers are ranked by biological pathway, with coloured
525 background shading corresponding to biological grouping. The vertical red dashed line
526 indicates the mock-infected baseline (fold change = 1).
527
528 **Figure 6. SARS-CoV-2 variants induce distinct amino acid reprogramming in nasal epithelial**
529 **cells.**
530 (**A**) **Bar plot showing total amino acid abundance** (nmol/10^6 cells) relative to mock-infected
531 controls at 24 hpi.
532 (**B**) **Variant–metabolite interaction network** showing amino acids (green nodes) connected
533 to each SARS-CoV-2 variant (grey nodes). Edges represent directionality of regulation
534 compared to mock: red edges indicate increased levels (upregulation), blue edges indicate

535 decreased levels (down-regulation), and black edges indicate no change.

536 (**C**) **Heatmap of log_2-transformed amino acid levels** (based on nmol/10^6 cells) for each

537 variant relative to mock-infected controls at 24 hpi. for each variant relative to mock-

538 infected controls at 24 hpi. Amino acids are annotated by metabolic pathway (left colour

539 bar) and biochemical role (right colour bar). Red shading indicates increased amino acid

540 abundance, and blue shading indicates decreased abundance**.**

541 **(D) Violin plots showing the % relative amino acid composition** after normalisation of each

542 amino acid to the total amino acid content within the same condition. This representation

543 highlights the internal proportional balance of amino acids rather than total abundance. The

544 black line indicates the median value for each distribution.

545

546

547

548

549 **MATERIALS AND METHODS**

550 **Cells and viruses**

551 Human nasal airway epithelial cells (NEC)s, maintained at the air–liquid interface

552 (MucilAir™, pooled from 14 donors, catalog no. EP02MP), were obtained in three batches

553 from Epithelix and cultured in MucilAir™ cell culture medium (Epithelix) at 37 °C with 5%

554 CO_2. SARS-CoV-2 variants were propagated and titrated as previously (Ogunjinmi *et al.*,

555 2024; Zhang *et al.*, 2022) in African green monkey kidney (VeroE6) cells expressing human

556 angiotensin-converting enzyme 2 (ACE2) and transmembrane protease serine 2 precursor

557 (TMPRSS2) (VAT), kindly provided by the MRC-University of Glasgow Centre for Virus

558 Research, Glasgow (Rihn *et al*., 2021). VAT cells were maintained in Dulbecco's Modified

559 Eagle Medium (DMEM) supplemented with 10% fetal calf serum (FCS), 1 mg/mL Geneticin
560 (Gibco), and 0.2 mg/mL Hygromycin B (Invitrogen). Viral stocks were generated and titrated
561 in VAT cells for the following SARS-CoV-2 variants: wild-type/D614G (hCoV-
562 19/England/IC19/2020, B.1.13, EPI_ISL_475572), Alpha (hCoV-19/England/205080610/2020,
563 B.1.1.7, EPI_ISL_723001), Delta (hCoV-19/England/SHEF-10E8F3B/2021, B.1.617.2,
564 EPI_ISL_1731019), Omicron BA.1 (hCoV-19/England/M21021166/2022, BA.1), and BA.5
565 (hCoV-19/England/NWLP_53/2022, BA.5).
566
567 **RNA-sequencing of nasal airway epithelial cells infected with SARS-CoV-2 variants**
568 Before infection, NEC cultures were washed with serum-free medium to remove mucus and
569 debris. Cells were then infected with 200 µL of virus-containing serum-free DMEM (MOI: 0.01)
570 and incubated at 37 °C for 1 hour. Following incubation, the inoculum was removed, and the
571 cells were washed twice. Time points were collected by adding 200 µL of serum-free DMEM,
572 incubating at 37 °C for 10 minutes, and then removing the medium for titration. Cells were
573 harvested at 24 and 72 hours for RNA isolation using the RNeasy Mini Plus kit (Qiagen), and
574 approximately 1 µg of RNA was used for sequencing library preparation.
575 mRNA libraries were prepared using poly-A enrichment and sequenced by Novogene. The
576 sequencing data (FASTQ raw files) were imported into Partek Flow (version 10.0, build
577 10.0.23.0531; Partek Inc.) for quality control and processing. Paired-end reads were trimmed
578 based on a Phred quality score threshold of >20 and aligned to the human genome (hg38)
579 using the STAR-2.7.8a aligner. Gene expression was quantified using the Ensembl Transcripts
580 release 104 v2 transcript model, and data were normalised using the counts per million (CPM)
581 method. Differential gene expression analysis was conducted using the DESeq2 package, with
582 genes considered differentially expressed if they met the criteria of FDR ≤ 0.05 and a log2 fold

583 change ≥ |1|. All RNA-seq data have been deposited in the Gene Expression Omnibus (GEO)
584 under accession number GSE271378.
585
586 **Pathway enrichment and transcriptomic profiling**
587 Normalised enrichment scores (NES) generated from the fGSEA analysis were visualised using
588 dot plots in R (v4.3) with the *ggplot2* (v3.4.4), *dplyr*, *tidyr*, *stringr*, and *readxl* packages. Each
589 dot represented a metabolic pathway under a specific condition, where the horizontal axis
590 denoted NES magnitude and the vertical axis listed the curated gene sets (cytosolic,
591 mitochondrial, and oxidative phosphorylation). Dot colour indicated the direction of
592 regulation (red, up-regulated; blue, down-regulated), and dot size was proportional to the
593 absolute NES value. Vertical reference lines at NES = 0 were included to indicate neutral
594 enrichment.
595 To aid visual interpretation, NES magnitudes were categorised as limited (|NES| < 1.0),
596 moderate (1.0 ≤ |NES| < 1.8), or strong (|NES| ≥ 1.8) enrichment. Only pathways meeting the
597 inclusion criteria defined in the differential expression analysis were displayed. While the dot
598 plots provide a comparative overview of pathway-level regulation, they represent aggregate
599 enrichment statistics rather than individual gene contributions. Adjusted *p*-values and false
600 discovery rates (FDR) computed during fGSEA were not visualised in the figure but are
601 reported in Supplementary Table S2. Pathway sizes (number of genes per set) and inter-gene
602 variance were not displayed to maintain visual clarity; therefore, pathways of different gene-
603 set sizes appear equally weighted. Similarly, replicate-level variability and confidence
604 intervals for NES values were not plotted, as the scores reflect ranked enrichment rather than
605 absolute expression magnitude. Relationships between overlapping pathways were not
606 visualised but were accounted for during pathway curation. Together, these dot plots

607 summarise the direction and magnitude of metabolic pathway enrichment across SARS-CoV-
608 2 variants and time points while maintaining a uniform visual scale for comparative
609 assessment.
610
611 **Quantification of viral and host gene expression by RT-qPCR**
612 Virus genome quantification was carried out using *E* gene RT-qPCR, following a previously
613 described method (Zhou *et al.*, 2022). Viral RNA was extracted from swab supernatant
614 samples using the QIAsymphony DSP Virus/Pathogen Mini Kit on the QIAsymphony
615 instrument (Qiagen). RT-qPCR was performed with the AgPath RT-PCR kit (Life Technologies)
616 on a QuantStudio 7 Flex Real-Time PCR System, using primers specific to the SARS-CoV-2 *E*
617 gene (Corman *et al.*, 2020). For absolute quantification of *E* gene RNA copies, a standard curve
618 was generated from serial dilutions of viral RNA with a known copy number. The *E* gene copies
619 per ml of the original virus supernatant were then determined based on this standard curve.
620
621 **Validation of RNA-sequencing data by quantitative RT-PCR**
622 To validate differential gene expression observed in RNA-seq, we performed quantitative
623 RT-PCR (qPCR) using independently designed primers as before (Giotis et al., 2019;
624 Ogunjinmi *et al.*, 2024; Zhang *et al.*, 2022). Genes were selected based on their
625 transcriptional regulation across SARS-CoV-2 variants and their relevance to innate immune
626 signalling (e.g., *CXCL10, IFIT1, IFIT2*, *ISG15*, *OAS1, STAT1*) or metabolic pathways (e.g., *HK2*,
627 *GMPR, MDH1B*, *ENO2, ATP6V1B1*). Total RNA was extracted from nasal epithelial cell
628 cultures using TRIzol™ Reagent (Fisher Scientific) according to the manufacturer's protocol.
629 qPCR was carried out on a CFX96 Real-Time PCR System (Bio-Rad) using PowerUp™ SYBR
630 Green Master Mix (Fisher Scientific). All reactions were run in triplicate to ensure

631 reproducibility. Primer sequences, designed based on NCBI RefSeq transcripts, are listed in
632 Table S5.
633
634 **Phospho-kinase array and signalling analysis**
635 Phosphorylation profiling was carried out using the Proteome Profiler Human Phospho-Kinase
636 Array Kit (ARY003B, R&D Systems), which detects phosphorylation at 43 kinase sites across
637 multiple host signalling pathways. Arrays were performed on lysates collected at 24 hpi from
638 the same nasal epithelial cell cultures used for transcriptomic and amino acid profiling,
639 ensuring matched experimental conditions across assays. Following protein extraction, total
640 protein was quantified using the Pierce BCA Protein Assay Kit (Thermo Scientific), and equal
641 amounts of lysate were incubated with array membranes overnight at 4 °C, according to the
642 manufacturer's instructions. Chemiluminescent signals were developed using SuperSignal
643 West Femto substrate (Thermo Scientific) and imaged with the Invitrogen iBright FL1500
644 system. Spot intensities were quantified in ImageJ (v1.53), corrected for background, and
645 normalised to internal reference spots. Fold changes were calculated relative to mock-
646 infected controls. Each condition was assessed in at least two independent experiments. Data
647 visualisation was performed in Python (v3.10) using seaborn and matplotlib. Phosphorylation
648 sites were grouped by pathway (e.g., PI3K-Akt, MAPK, JAK-STAT) based on KEGG and
649 Reactome annotations (Figure 5). Dot plots represent mean fold changes ± SEM, with the
650 mock baseline shown as a red dashed line.
651
652
653
654

655 **Quantitative amino acid profiling and network-based visualisation of metabolic disruption**

656 Amino acid analysis was performed using hydrophilic interaction chromatography-tandem
657 mass spectrometry (HILIC-MS/MS), similar as previously described (Jeffares *et al.*, 2015;
658 Mulleder *et al.*, 2017; Rallis *et al.*, 2021). We used four biological replicates per condition,
659 each processed in duplicate (two technical replicates), to ensure robustness and
660 reproducibility of quantification. One million cells were harvested per condition (mock and
661 viral infections). For extraction, cells were pelleted (3000g, 3 min), washed briefly, and
662 resuspended in 200 µL of 80% ethanol preheated to 80 °C. The suspension was vortexed and
663 incubated at 80 °C for 2 minutes, repeated once, then centrifuged at maximum speed for 2
664 minutes to clear cell debris and stored at 80 °C until further usage. For the exact amino acid
665 quantification, we included cell free $^{15}N^{13}C$ labelled amino acids as internal standard (CNLM-
666 6696-PK, Cambridge Isotope Laboratories). Besides, a calibration curve was generated using
667 serial dilutions of standards. The amino acid measurements were performed by using a
668 flowrate of 0.6 ml/min for 12 min. All proteinogenic amino acids amino expect cysteine were
669 measured.

670 Final amino acid concentrations were expressed as nanomoles (nmol) per 10^6 cells to
671 normalise for input cell number across conditions (Table S4).

672 To visualise SARS-CoV-2 variant-specific amino acid expression changes, a bipartite node
673 network was constructed using Python (pandas, numpy, networkx, matplotlib). Amino acid
674 $\log_2$ fold changes relative to mock at 24 hpi (Table S4) were used to identify the top five most
675 dysregulated amino acids per variant (ranked by absolute $\log_2$ fold change). These variant–
676 amino acid pairs formed the network edges. Edge thickness reflected the magnitude of the
677 change, while colour indicated direction: red (increased abundance), blue (decreased
678 abundance), and black (no substantial change). Amino acid nodes were sized by total

679 connectivity and coloured according to their dominant direction of change across variants.
680 The layout was manually optimised for clarity. This network allowed integrated visualisation
681 of shared and distinct metabolic disruptions across variants, complementing the
682 quantitative $\log_2$ fold-change data presented in heatmaps.

683 **Statistical analysis**

684 All data were analysed using GraphPad Prism software (v9) and Python (v3.10). Results are
685 presented as mean ± SEM. Statistical significance was defined as $p < 0.05$, with levels of
686 significance indicated as follows: $p < 0.05$ (*), $p < 0.01$ (**), and $p < 0.001$ (***).

687 To assess differences in viral replication between SARS-CoV-2 variants at each time point
688 relative to the reference strain IC19, a one-way ANOVA was performed at 0, 24, 48, and 72
689 hpi. If statistical significance ($p < 0.05$) was observed, Tukey's Honest Significant Difference
690 (HSD) test was conducted for post-hoc pairwise comparisons to determine specific
691 differences between IC19 and each variant. Adjusted p-values from Tukey's HSD test were
692 used to control for multiple comparisons, ensuring robust identification of significant
693 replication differences. Variants exhibiting p-values below the 0.05 threshold were
694 considered to have significant replication advantages or disadvantages relative to IC19.
695 Results were annotated on viral growth curves to highlight meaningful differences across the
696 infection timeline.

697 Phospho-array data were log-transformed data and analysed using Welch's t-tests, followed
698 by Benjamini-Hochberg correction for multiple comparisons (Table S4). Amino acid
699 concentrations (nmol per 10^6 cells) were measured in four biological replicates per condition,
700 each processed in duplicate. Technical replicates were averaged per biological replicate
701 before statistical analysis. For each amino acid, mean values were used to calculate the fold
702 change relative to mock and the corresponding $\log_2$ fold change ($\log_2FC = \log_2[\text{variant}/\text{mock}]$).

703 Statistical testing was performed using Welch's two-sample t-tests (unequal variances)
704 applied to each amino acid for: (i) comparisons of each SARS-CoV-2 variant against mock, and
705 (ii) all pairwise comparisons between conditions (mock, IC19, Delta, BA.1, BA.5). Multiple
706 testing within each comparison was corrected using the Benjamini–Hochberg false discovery
707 rate (FDR) procedure (threshold $q < 0.05$). Table S4 reports, for each amino acid and
708 comparison, the raw p value, the FDR-adjusted q value, a Yes/No column indicating
709 significance at $q < 0.05$, and p-value significance symbols (* $p < 0.05$; ** $p < 0.01$; *** $p <$
710 0.001; **** $p < 0.0001$; ns for non-significant). Log_2FC values are provided as effect sizes.
711 To assess whether infection altered amino acid composition independently of total
712 abundance, amino acid levels were normalised to the total amino acid content within each
713 condition. The resulting relative proportions were compared across variants using the
714 Friedman test with Dunn's multiple-comparison correction (GraphPad Prism v9). Total amino
715 acid abundance per condition was calculated by summing per–amino acid means, with
716 percent change expressed relative to Mock.

717 **Data visualisation**

718 To illustrate shifts in amino acid levels across SARS-CoV-2 variants, heatmaps and summary
719 tables were used to facilitate interpretation and guide RNA-seq pathway analysis. For
720 phosphoproteomic analyses, heatmaps were generated using Python's matplotlib and
721 seaborn libraries. Heatmap of amino acid fold changes were generated using
722 the pheatmap package in R (v4.3), clustering both rows and columns to reveal variant-specific
723 metabolite patterns. Venn diagrams were created with InteractiVenn (Heberle *et al.*, 2015) to
724 analyse shared and unique features across different conditions.

725

726 **References**

Allen, C.N.S., Arjona, S.P., Santerre, M., and Sawaya, B.E. (2022). Hallmarks of Metabolic Reprogramming and Their Role in Viral Pathogenesis. Viruses *14*. 10.3390/v14030602.

Bojkova, D., Klann, K., Koch, B., Widera, M., Krause, D., Ciesek, S., Cinatl, J., and Munch, C. (2020). Proteomics of SARS-CoV-2-infected host cells reveals therapy targets. Nature *583*, 469-472. 10.1038/s41586-020-2332-7.

Bouhaddou, M., Memon, D., Meyer, B., White, K.M., Rezelj, V.V., Correa Marrero, M., Polacco, B.J., Melnyk, J.E., Ulferts, S., Kaake, R.M., et al. (2020). The Global Phosphorylation Landscape of SARS-CoV-2 Infection. Cell *182*, 685-712 e619. 10.1016/j.cell.2020.06.034.

Carabelli, A.M., Peacock, T.P., Thorne, L.G., Harvey, W.T., Hughes, J., Consortium, C.-G.U., Peacock, S.J., Barclay, W.S., de Silva, T.I., Towers, G.J., and Robertson, D.L. (2023). SARS-CoV-2 variant biology: immune escape, transmission and fitness. Nat Rev Microbiol *21*, 162-177. 10.1038/s41579-022-00841-7.

Chan, E.Y., Sutton, J.N., Jacobs, J.M., Bondarenko, A., Smith, R.D., and Katze, M.G. (2009). Dynamic host energetics and cytoskeletal proteomes in human immunodeficiency virus type 1-infected human primary CD4 cells: analysis by multiplexed label-free mass spectrometry. J Virol *83*, 9283-9295. 10.1128/JVI.00814-09.

Codo, A.C., Davanzo, G.G., Monteiro, L.B., de Souza, G.F., Muraro, S.P., Virgilio-da-Silva, J.V., Prodonoff, J.S., Carregari, V.C., de Biagi Junior, C.A.O., Crunfli, F., et al. (2020). Elevated Glucose Levels Favor SARS-CoV-2 Infection and Monocyte Response through a HIF-1alpha/Glycolysis-Dependent Axis. Cell Metab *32*, 437-446 e435. 10.1016/j.cmet.2020.07.007.

Corman, V.M., Landt, O., Kaiser, M., Molenkamp, R., Meijer, A., Chu, D.K., Bleicker, T., Brunink, S., Schneider, J., Schmidt, M.L., et al. (2020). Detection of 2019 novel coronavirus (2019-nCoV) by real-time RT-PCR. Euro Surveill *25*. 10.2807/1560-7917.ES.2020.25.3.2000045.

Desmyter, J., Melnick, J.L., and Rawls, W.E. (1968). Defectiveness of interferon production and of rubella virus interference in a line of African green monkey kidney cells (Vero). J Virol *2*, 955-961. 10.1128/JVI.2.10.955-961.1968.

Giotis, E.S., Carnell, G., Young, E.F., Ghanny, S., Soteropoulos, P., Wang, L.F., Barclay, W.S., Skinner, M.A., and Temperton, N. (2019). Entry of the bat influenza H17N10 virus into mammalian cells is enabled by the MHC class II HLA-DR receptor. Nat Microbiol *4*, 2035-2038. 10.1038/s41564-019-0517-3.

Giotis, E.S., Cil, E., and Brooke, G.N. (2022). Use of Antiandrogens as Therapeutic Agents in COVID-19 Patients. Viruses *14*. 10.3390/v14122728.

Gori Savellini, G., Anichini, G., and Cusi, M.G. (2023). SARS-CoV-2 omicron sub-lineages differentially modulate interferon response in human lung epithelial cells. Virus Res *332*, 199134. 10.1016/j.virusres.2023.199134.

Guarnieri, J.W., Haltom, J.A., Albrecht, Y.E.S., Lie, T., Olali, A.Z., Widjaja, G.A., Ranshing, S.S., Angelin, A., Murdock, D., and Wallace, D.C. (2024). SARS-CoV-2 mitochondrial metabolic and epigenomic reprogramming in COVID-19. Pharmacol Res *204*, 107170. 10.1016/j.phrs.2024.107170.

Harvey, W.T., Carabelli, A.M., Jackson, B., Gupta, R.K., Thomson, E.C., Harrison, E.M., Ludden, C., Reeve, R., Rambaut, A., Consortium, C.-G.U., et al. (2021). SARS-CoV-2 variants, spike mutations and immune escape. Nat Rev Microbiol *19*, 409-424. 10.1038/s41579-021-00573-0.

Heberle, H., Meirelles, G.V., da Silva, F.R., Telles, G.P., and Minghim, R. (2015). InteractiVenn: a web-based tool for the analysis of sets through Venn diagrams. BMC Bioinformatics *16*, 169. 10.1186/s12859-015-0611-3.

773 Jeffares, D.C., Rallis, C., Rieux, A., Speed, D., Prevorovsky, M., Mourier, T., Marsellach, F.X.,
774 Iqbal, Z., Lau, W., Cheng, T.M., et al. (2015). The genomic and phenotypic diversity of
775 Schizosaccharomyces pombe. Nat Genet *47*, 235-241. 10.1038/ng.3215.
776 Klann, K., Bojkova, D., Tascher, G., Ciesek, S., Munch, C., and Cinatl, J. (2020). Growth Factor
777 Receptor Signaling Inhibition Prevents SARS-CoV-2 Replication. Mol Cell *80*, 164-174 e164.
778 10.1016/j.molcel.2020.08.006.
779 Laine, L., Skon, M., Vaisanen, E., Julkunen, I., and Osterlund, P. (2022). SARS-CoV-2 variants
780 Alpha, Beta, Delta and Omicron show a slower host cell interferon response compared to an
781 early pandemic variant. Front Immunol *13*, 1016108. 10.3389/fimmu.2022.1016108.
782 Leach, D.A., Mohr, A., Giotis, E.S., Cil, E., Isac, A.M., Yates, L.L., Barclay, W.S., Zwacka, R.M.,
783 Bevan, C.L., and Brooke, G.N. (2021). The antiandrogen enzalutamide downregulates
784 TMPRSS2 and reduces cellular entry of SARS-CoV-2 in human lung cells. Nat Commun *12*,
785 4068. 10.1038/s41467-021-24342-y.
786 Li, F., Li, J., Wang, P.H., Yang, N., Huang, J., Ou, J., Xu, T., Zhao, X., Liu, T., Huang, X., et al. (2021).
787 SARS-CoV-2 spike promotes inflammation and apoptosis through autophagy by ROS-
788 suppressed PI3K/AKT/mTOR signaling. Biochim Biophys Acta Mol Basis Dis *1867*, 166260.
789 10.1016/j.bbadis.2021.166260.
790 Liu, P.J., Harris, J.M., Marchi, E., D'Arienzo, V., Michler, T., Wing, P.A.C., Magri, A., Ortega-Prieto,
791 A.M., van de Klundert, M., Wettengel, J., et al. (2020). Hypoxic gene expression in chronic
792 hepatitis B virus infected patients is not observed in state-of-the-art in vitro and mouse
793 infection models. Sci Rep *10*, 14101. 10.1038/s41598-020-70865-7.
794 Liu, Y., and Rocklov, J. (2021). The reproductive number of the Delta variant of SARS-CoV-2 is
795 far higher compared to the ancestral SARS-CoV-2 virus. J Travel Med *28*. 10.1093/jtm/taab124.
796 Long, J.S., Giotis, E.S., Moncorge, O., Frise, R., Mistry, B., James, J., Morisson, M., Iqbal, M.,
797 Vignal, A., Skinner, M.A., and Barclay, W.S. (2016). Species difference in ANP32A underlies
798 influenza A virus polymerase host restriction. Nature *529*, 101-104. 10.1038/nature16474.
799 Mulleder, M., Bluemlein, K., and Ralser, M. (2017). A High-Throughput Method for the
800 Quantitative Determination of Free Amino Acids in Saccharomyces cerevisiae by Hydrophilic
801 Interaction Chromatography-Tandem Mass Spectrometry. Cold Spring Harb Protoc *2017*, pdb
802 prot089094. 10.1101/pdb.prot089094.
803 Mullen, P.J., Garcia, G., Jr., Purkayastha, A., Matulionis, N., Schmid, E.W., Momcilovic, M., Sen,
804 C., Langerman, J., Ramaiah, A., Shackelford, D.B., et al. (2021). SARS-CoV-2 infection rewires
805 host cell metabolism and is potentially susceptible to mTORC1 inhibition. Nat Commun *12*,
806 1876. 10.1038/s41467-021-22166-4.
807 Ogunjinmi, O.D., Abdullahi, T., Somji, R.A., Bevan, C.L., Barclay, W.S., Temperton, N., Brooke,
808 G.N., and Giotis, E.S. (2024). The antiviral potential of the antiandrogen enzalutamide and the
809 viral-androgen signaling interplay in seasonal coronaviruses. J Med Virol *96*, e29540.
810 10.1002/jmv.29540.
811 Park, A., and Iwasaki, A. (2020). Type I and Type III Interferons - Induction, Signaling, Evasion,
812 and Application to Combat COVID-19. Cell Host Microbe *27*, 870-878.
813 10.1016/j.chom.2020.05.008.
814 Polcicova, K., Badurova, L., and Tomaskova, J. (2020). Metabolic reprogramming as a feast for
815 virus replication. Acta Virol *64*, 201-215. 10.4149/av_2020_210.
816 Rajah, M.M., Hubert, M., Bishop, E., Saunders, N., Robinot, R., Grzelak, L., Planas, D., Dufloo,
817 J., Gellenoncourt, S., Bongers, A., et al. (2021). SARS-CoV-2 Alpha, Beta, and Delta variants
818 display enhanced Spike-mediated syncytia formation. EMBO J *40*, e108944.
819 10.15252/embj.2021108944.

Rallis, C., Mulleder, M., Smith, G., Au, Y.Z., Ralser, M., and Bahler, J. (2021). Amino Acids Whose Intracellular Levels Change Most During Aging Alter Chronological Life Span of Fission Yeast. J Gerontol A Biol Sci Med Sci *76*, 205-210. 10.1093/gerona/glaa246.

Reuschl, A.K., Thorne, L.G., Whelan, M.V.X., Ragazzini, R., Furnon, W., Cowton, V.M., De Lorenzo, G., Mesner, D., Turner, J.L.E., Dowgier, G., et al. (2024). Evolution of enhanced innate immune suppression by SARS-CoV-2 Omicron subvariants. Nat Microbiol *9*, 451-463. 10.1038/s41564-023-01588-4.

Rihn, S.J., Merits, A., Bakshi, S., Turnbull, M.L., Wickenhagen, A., Alexander, A.J.T., Baillie, C., Brennan, B., Brown, F., Brunker, K., et al. (2021). A plasmid DNA-launched SARS-CoV-2 reverse genetics system and coronavirus toolkit for COVID-19 research. PLoS Biol *19*, e3001091. 10.1371/journal.pbio.3001091.

Ritter, J.B., Wahl, A.S., Freund, S., Genzel, Y., and Reichl, U. (2010). Metabolic effects of influenza virus infection in cultured animal cells: Intra- and extracellular metabolite profiling. BMC Syst Biol *4*, 61. 10.1186/1752-0509-4-61.

Schneider, W.M., Chevillotte, M.D., and Rice, C.M. (2014). Interferon-stimulated genes: a complex web of host defenses. Annu Rev Immunol *32*, 513-545. 10.1146/annurev-immunol-032713-120231.

Schoggins, J.W. (2019). Interferon-Stimulated Genes: What Do They All Do? Annu Rev Virol *6*, 567-584. 10.1146/annurev-virology-092818-015756.

Schoggins, J.W., Wilson, S.J., Panis, M., Murphy, M.Y., Jones, C.T., Bieniasz, P., and Rice, C.M. (2011). A diverse range of gene products are effectors of the type I interferon antiviral response. Nature *472*, 481-485. 10.1038/nature09907.

Shi, G., Li, T., Lai, K.K., Johnson, R.F., Yewdell, J.W., and Compton, A.A. (2024). Omicron Spike confers enhanced infectivity and interferon resistance to SARS-CoV-2 in human nasal tissue. Nat Commun *15*, 889. 10.1038/s41467-024-45075-8.

Sievers, B.L., Cheng, M.T.K., Csiba, K., Meng, B., and Gupta, R.K. (2024). SARS-CoV-2 and innate immunity: the good, the bad, and the "goldilocks". Cell Mol Immunol *21*, 171-183. 10.1038/s41423-023-01104-y.

Singh, M., Bansal, V., and Feschotte, C. (2020). A Single-Cell RNA Expression Map of Human Coronavirus Entry Factors. Cell Rep *32*, 108175. 10.1016/j.celrep.2020.108175.

Sposito, B., Broggi, A., Pandolfi, L., Crotta, S., Clementi, N., Ferrarese, R., Sisti, S., Criscuolo, E., Spreafico, R., Long, J.M., et al. (2021). The interferon landscape along the respiratory tract impacts the severity of COVID-19. Cell *184*, 4953-4968 e4916. 10.1016/j.cell.2021.08.016.

Sungnak, W., Huang, N., Becavin, C., Berg, M., Queen, R., Litvinukova, M., Talavera-Lopez, C., Maatz, H., Reichart, D., Sampaziotis, F., et al. (2020). SARS-CoV-2 entry factors are highly expressed in nasal epithelial cells together with innate immune genes. Nat Med *26*, 681-687. 10.1038/s41591-020-0868-6.

Tandel, D., Sah, V., Singh, N.K., Potharaju, P.S., Gupta, D., Shrivastava, S., Sowpati, D.T., and Harshan, K.H. (2022). SARS-CoV-2 Variant Delta Potently Suppresses Innate Immune Response and Evades Interferon-Activated Antiviral Responses in Human Colon Epithelial Cells. Microbiol Spectr *10*, e0160422. 10.1128/spectrum.01604-22.

Thaker, S.K., Ch'ng, J., and Christofk, H.R. (2019). Viral hijacking of cellular metabolism. BMC Biol *17*, 59. 10.1186/s12915-019-0678-9.

V'Kovski, P., Kratzel, A., Steiner, S., Stalder, H., and Thiel, V. (2021). Coronavirus biology and replication: implications for SARS-CoV-2. Nat Rev Microbiol *19*, 155-170. 10.1038/s41579-020-00468-6.

866 Yuen, C.K., Lam, J.Y., Wong, W.M., Mak, L.F., Wang, X., Chu, H., Cai, J.P., Jin, D.Y., To, K.K., Chan,
867 J.F., et al. (2020). SARS-CoV-2 nsp13, nsp14, nsp15 and orf6 function as potent interferon
868 antagonists. Emerg Microbes Infect *9*, 1418-1428. 10.1080/22221751.2020.1780953.
869 Zambalde, E.P., Dias, T.L., Maktura, G.C., Amorim, M.R., Brenha, B., Santos, L.N., Buscaratti, L.,
870 Elston, J.G.A., Mancini, M.C.S., Pavan, I.C.B., et al. (2022). Increased mTOR Signaling and
871 Impaired Autophagic Flux Are Hallmarks of SARS-CoV-2 Infection. Curr Issues Mol Biol *45*, 327-
872 336. 10.3390/cimb45010023.
873 Zhang, Z., Penn, R., Barclay, W.S., and Giotis, E.S. (2022). Naive Human Macrophages Are
874 Refractory to SARS-CoV-2 Infection and Exhibit a Modest Inflammatory Response Early in
875 Infection. Viruses *14*. 10.3390/v14020441.
876 Zhou, J., Peacock, T.P., Brown, J.C., Goldhill, D.H., Elrefaey, A.M.E., Penrice-Randal, R., Cowton,
877 V.M., De Lorenzo, G., Furnon, W., Harvey, W.T., et al. (2022). Mutations that adapt SARS-CoV-
878 2 to mink or ferret do not increase fitness in the human airway. Cell Rep *38*, 110344.
879 10.1016/j.celrep.2022.110344.

880

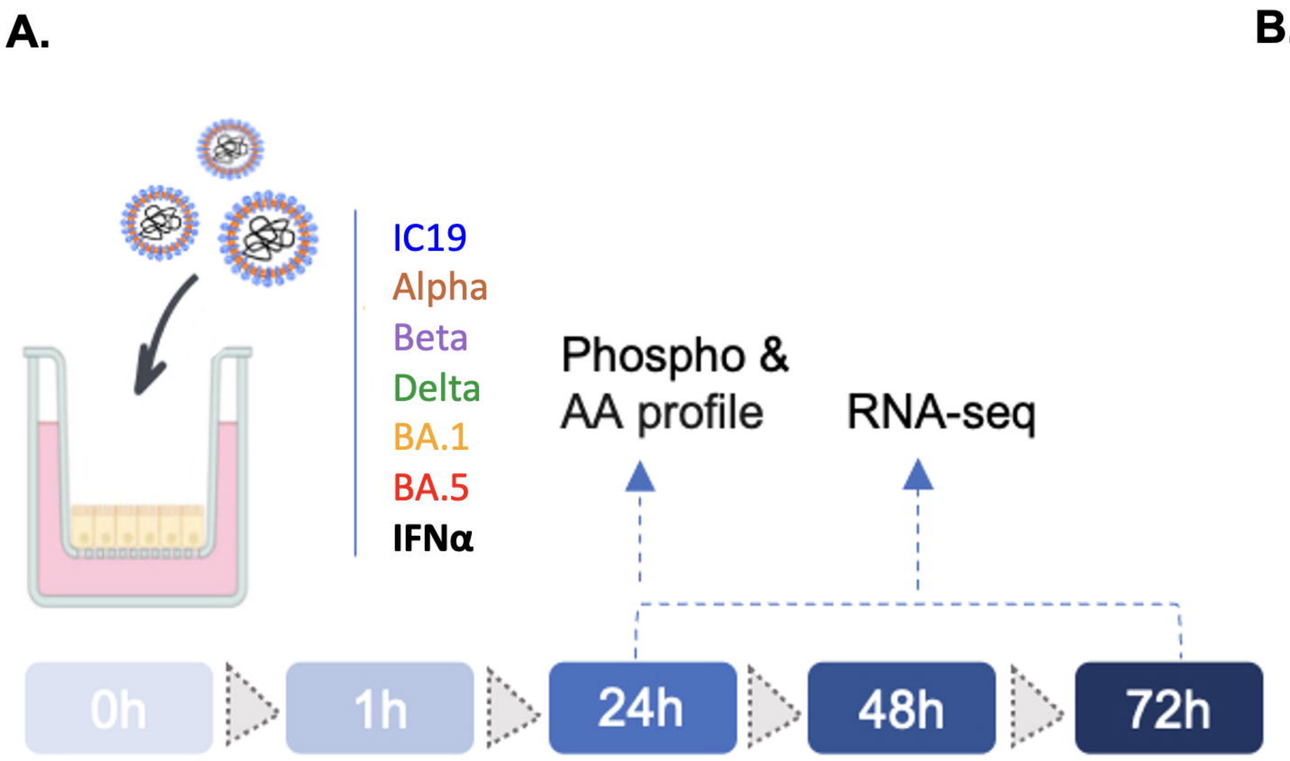
A.
IC19
Alpha
Beta
Delta
BA.1
BA.5
IFNα
Phospho &
AA profile
RNA-seq
0h
1h
24h
48h
72h

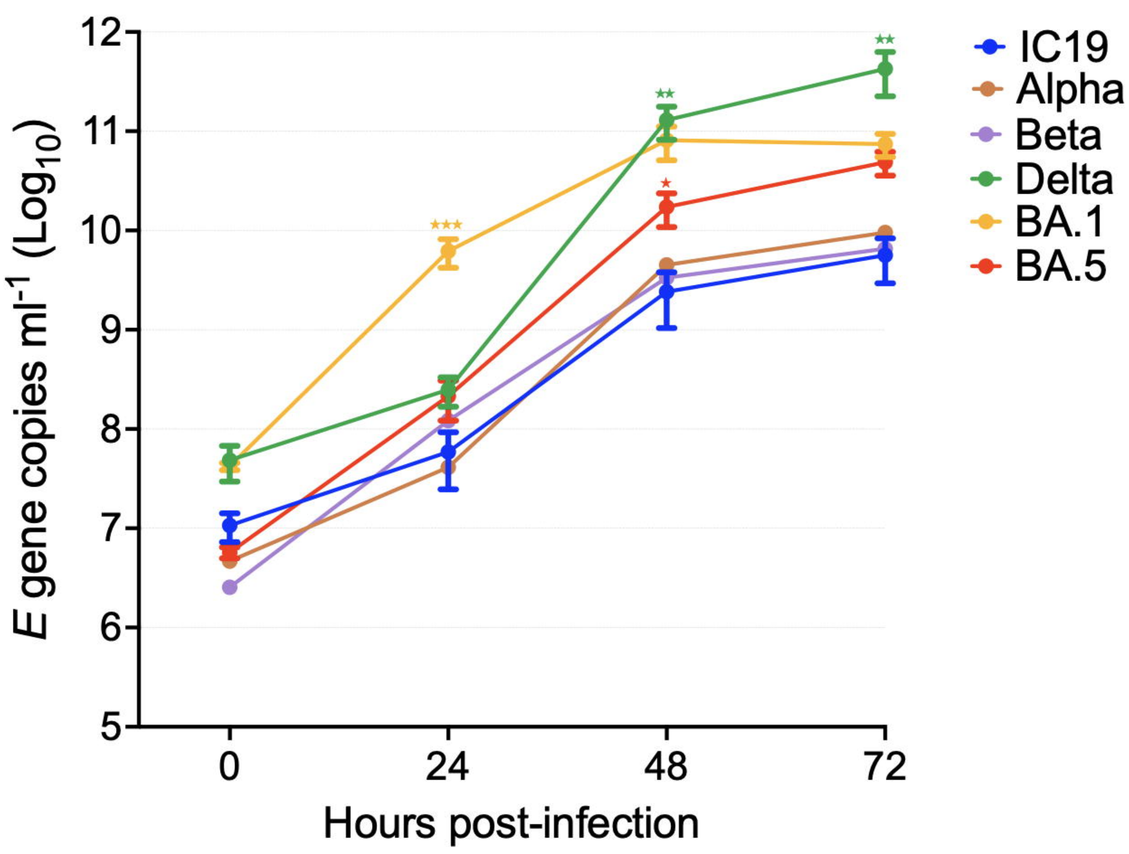
B.
E gene copies ml-1 (Log10)
12
11
10
9
8
7
6
5
0
24
48
72
Hours post-infection
IC19
Alpha
Beta
Delta
BA.1
BA.5

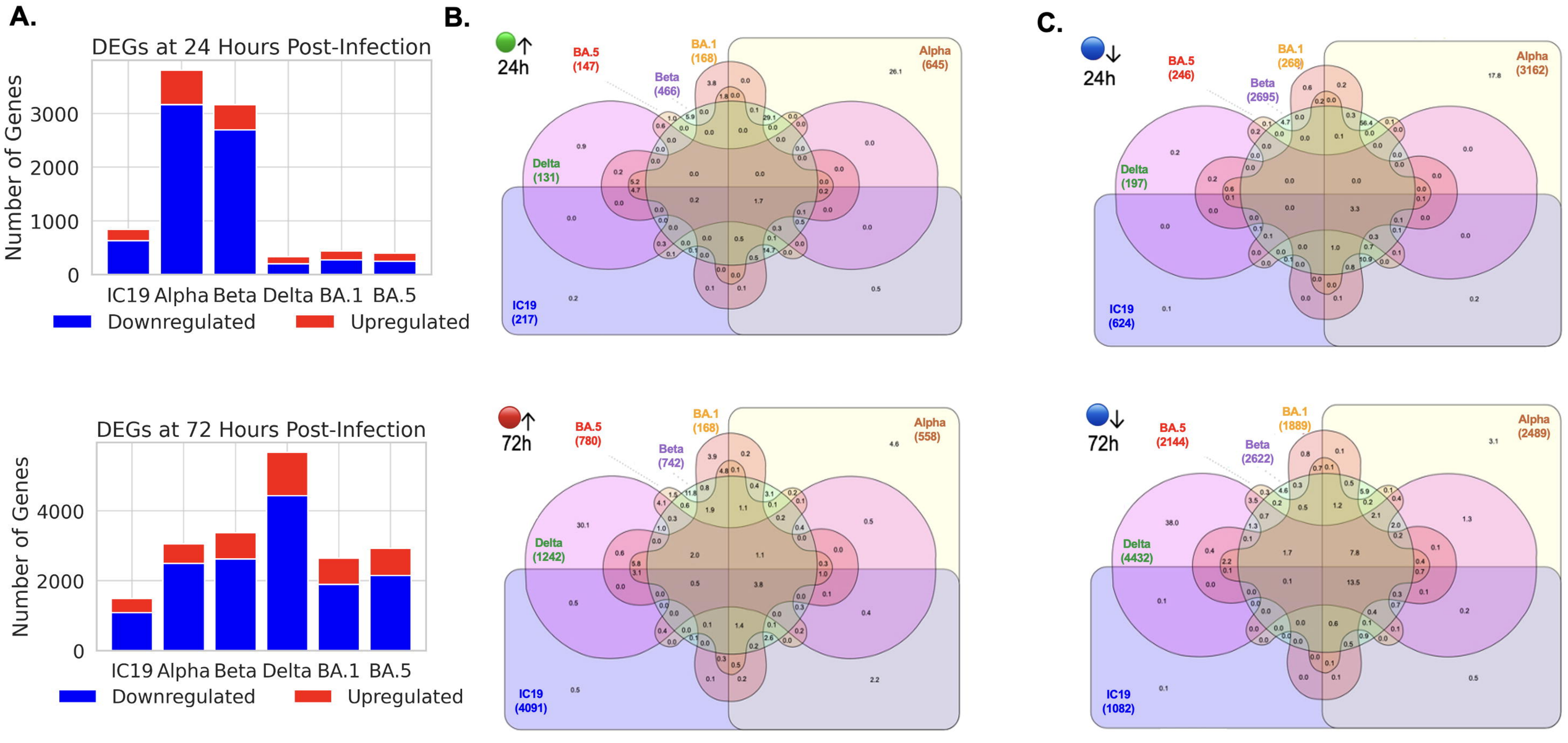
A.
DEGs at 24 Hours Post-Infection
Number of Genes
0
1000
2000
3000
IC19 Alpha Beta Delta BA.1 BA.5
Downregulated
Upregulated
DEGs at 72 Hours Post-Infection
Number of Genes
0
2000
4000
IC19 Alpha Beta Delta BA.1 BA.5
Downregulated
Upregulated
B.
24h
BA.5 (147)
BA.1 (168)
Beta (466)
Alpha (645)
Delta (131)
IC19 (217)
72h
BA.5 (780)
BA.1 (168)
Beta (742)
Alpha (558)
Delta (1242)
IC19 (4091)
C.
24h
BA.5 (246)
BA.1 (268)
Beta (2695)
Alpha (3162)
Delta (197)
IC19 (624)
72h
BA.5 (2144)
BA.1 (1889)
Beta (2622)
Alpha (2489)
Delta (4432)
IC19 (1082)

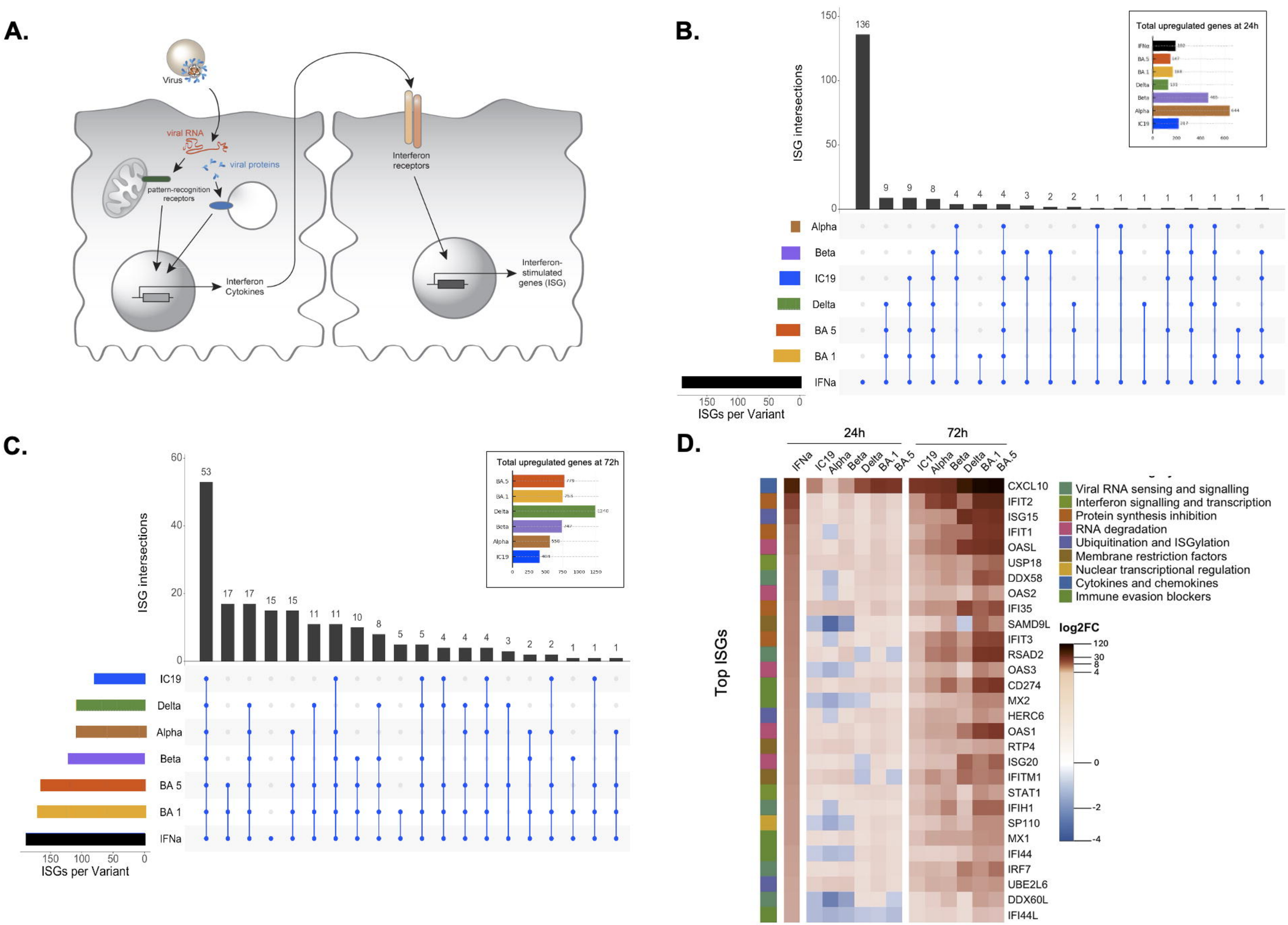
A.
Virus
viral RNA
viral proteins
pattern-recognition receptors
Interferon Cytokines
Interferon receptors
Interferon-stimulated genes (ISG)
B.
ISG intersections
Total upregulated genes at 24h
IFNa
BA.5
BA.1
Delta
Beta
Alpha
IC19
ISGs per Variant
C.
ISG intersections
Total upregulated genes at 72h
ISGs per Variant
D.
24h
72h
Top ISGs
CXCL10
IFIT2
ISG15
IFIT1
OASL
USP18
DDX58
OAS2
IFI35
SAMD9L
IFIT3
RSAD2
OAS3
CD274
MX2
HERC6
OAS1
RTP4
ISG20
IFITM1
STAT1
IFIH1
SP110
MX1
IFI44
IRF7
UBE2L6
DDX60L
IFI44L
Viral RNA sensing and signalling
Interferon signalling and transcription
Protein synthesis inhibition
RNA degradation
Ubiquitination and ISGylation
Membrane restriction factors
Nuclear transcriptional regulation
Cytokines and chemokines
Immune evasion blockers
log2FC

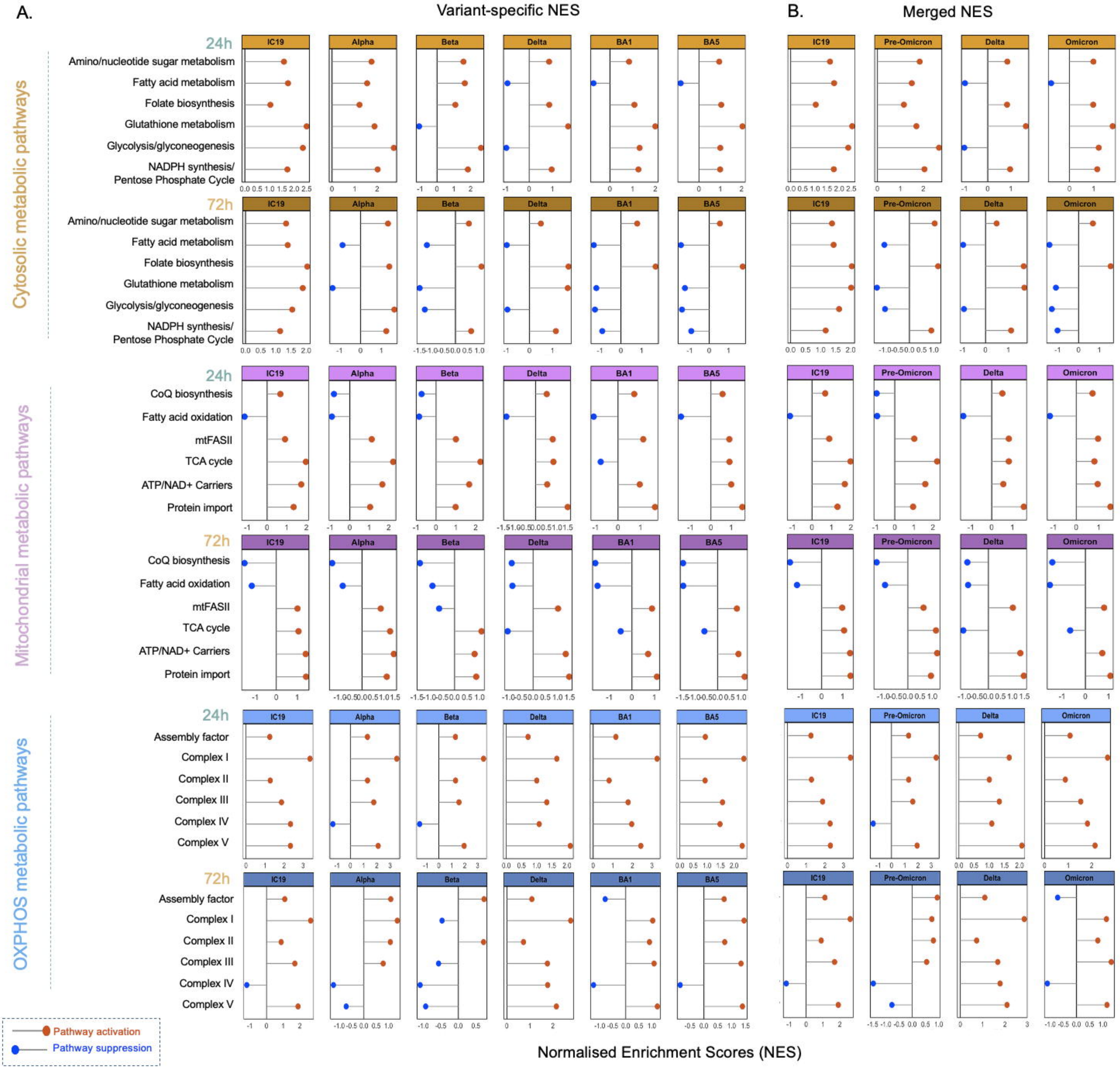
A.
Variant-specific NES
B.
Merged NES
Cytosolic metabolic pathways
24h
72h
Amino/nucleotide sugar metabolism
Fatty acid metabolism
Folate biosynthesis
Glutathione metabolism
Glycolysis/glyconeogenesis
NADPH synthesis/
Pentose Phosphate Cycle
Mitochondrial metabolic pathways
CoQ biosynthesis
Fatty acid oxidation
mtFASII
TCA cycle
ATP/NAD+ Carriers
Protein import
OXPHOS metabolic pathways
Assembly factor
Complex I
Complex II
Complex III
Complex IV
Complex V
IC19
Alpha
Beta
Delta
BA1
BA5
Pre-Omicron
Omicron
Pathway activation
Pathway suppression
Normalised Enrichment Scores (NES)

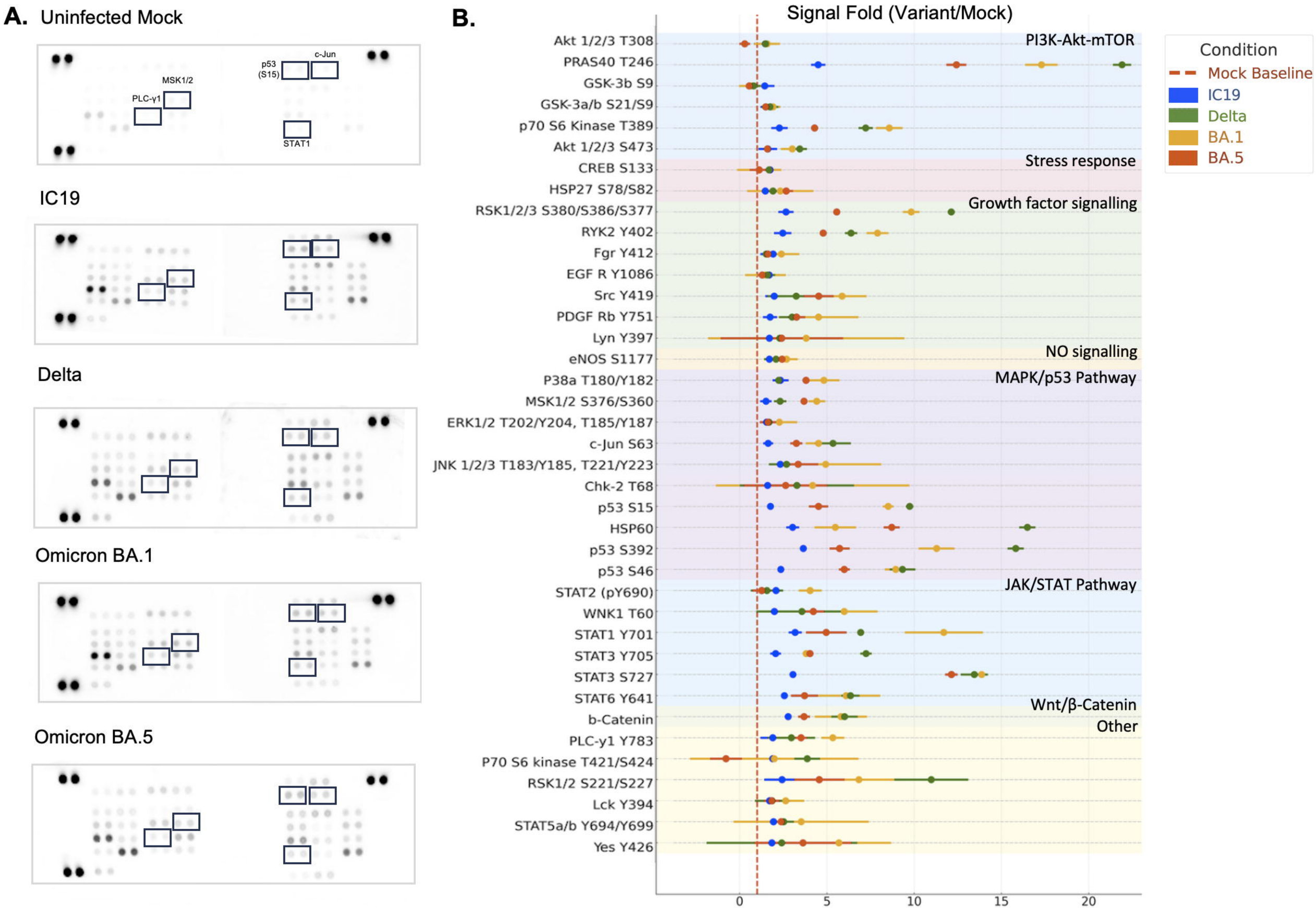
A.
Uninfected Mock
p53 (S15)
c-Jun
MSK1/2
PLC-γ1
STAT1
IC19
Delta
Omicron BA.1
Omicron BA.5
B.
Signal Fold (Variant/Mock)
Akt 1/2/3 T308
PRAS40 T246
GSK-3b S9
GSK-3a/b S21/S9
p70 S6 Kinase T389
Akt 1/2/3 S473
CREB S133
HSP27 S78/S82
RSK1/2/3 S380/S386/S377
RYK2 Y402
Fgr Y412
EGF R Y1086
Src Y419
PDGF Rb Y751
Lyn Y397
eNOS S1177
P38a T180/Y182
MSK1/2 S376/S360
ERK1/2 T202/Y204, T185/Y187
c-Jun S63
JNK 1/2/3 T183/Y185, T221/Y223
Chk-2 T68
p53 S15
HSP60
p53 S392
p53 S46
STAT2 (pY690)
WNK1 T60
STAT1 Y701
STAT3 Y705
STAT3 S727
STAT6 Y641
b-Catenin
PLC-y1 Y783
P70 S6 kinase T421/S424
RSK1/2 S221/S227
Lck Y394
STAT5a/b Y694/Y699
Yes Y426
PI3K-Akt-mTOR
Stress response
Growth factor signalling
NO signalling
MAPK/p53 Pathway
JAK/STAT Pathway
Wnt/β-Catenin
Other
0
5
10
15
20
Condition
Mock Baseline
IC19
Delta
BA.1
BA.5

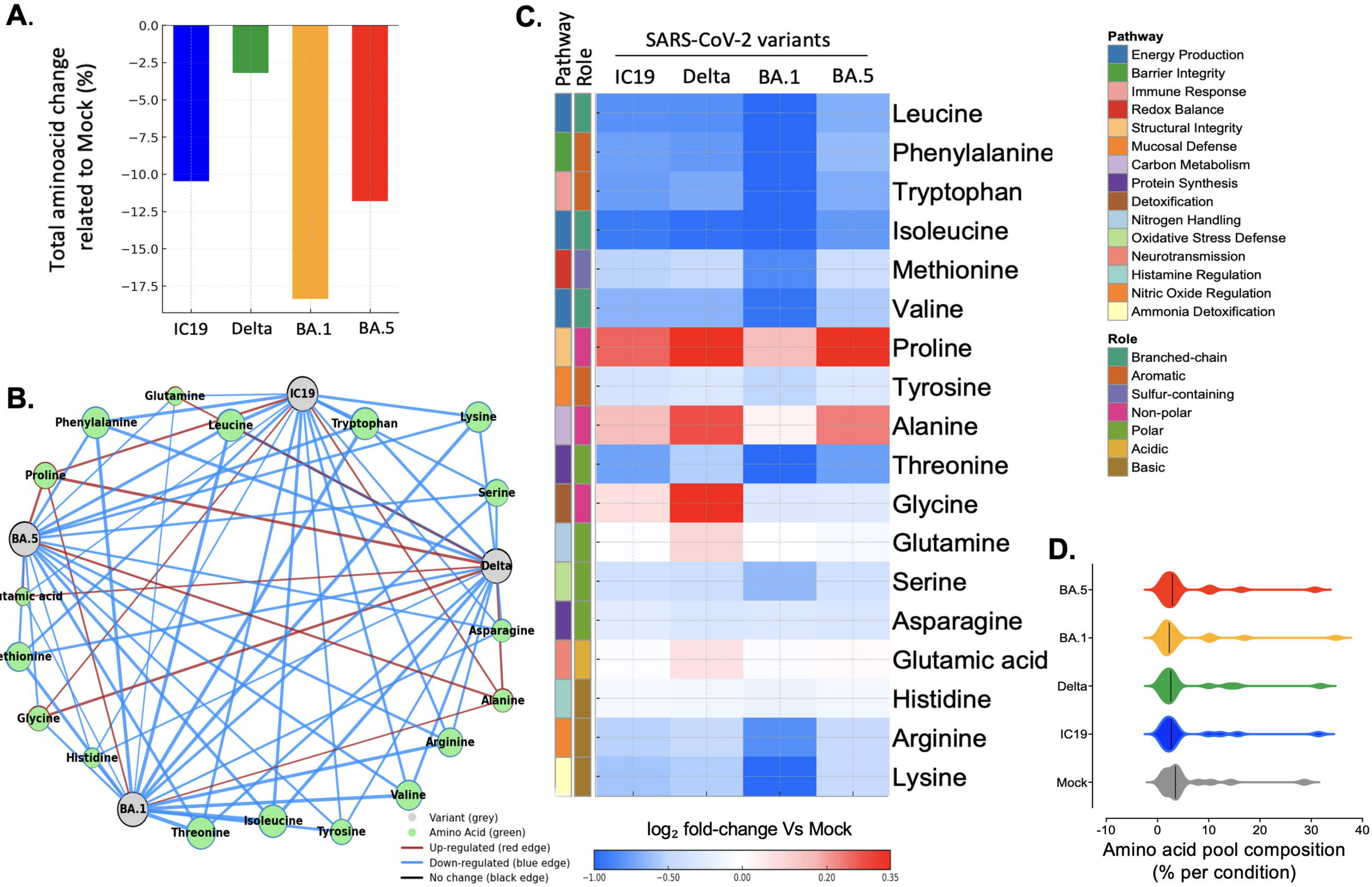
A.
Total aminoacid change related to Mock (%)
0.0
−2.5
−5.0
−7.5
−10.0
−12.5
−15.0
−17.5
IC19
Delta
BA.1
BA.5
B.
Glutamine
IC19
Phenylalanine
Leucine
Tryptophan
Lysine
Proline
Serine
BA.5
Delta
Glutamic acid
Asparagine
Methionine
Alanine
Glycine
Arginine
Histidine
Valine
BA.1
Isoleucine
Threonine
Tyrosine
Variant (grey)
Amino Acid (green)
Up-regulated (red edge)
Down-regulated (blue edge)
No change (black edge)
C.
Pathway
Role
SARS-CoV-2 variants
IC19
Delta
BA.1
BA.5
Leucine
Phenylalanine
Tryptophan
Isoleucine
Methionine
Valine
Proline
Tyrosine
Alanine
Threonine
Glycine
Glutamine
Serine
Asparagine
Glutamic acid
Histidine
Arginine
Lysine
log2 fold-change Vs Mock
−1.00
−0.50
0.00
0.20
0.35
Pathway
Energy Production
Barrier Integrity
Immune Response
Redox Balance
Structural Integrity
Mucosal Defense
Carbon Metabolism
Protein Synthesis
Detoxification
Nitrogen Handling
Oxidative Stress Defense
Neurotransmission
Histamine Regulation
Nitric Oxide Regulation
Ammonia Detoxification
Role
Branched-chain
Aromatic
Sulfur-containing
Non-polar
Polar
Acidic
Basic
D.
BA.5
BA.1
Delta
IC19
Mock
-10
0
10
20
30
40
Amino acid pool composition
(% per condition)